PHYSICAL REVIEW B **95**, 224426 (2017)

Magnetization dynamics of $Ni_{80}Fe_{20}$ nanowires with continuous width modulation

L. L. Xiong,[1] M. Kostylev,[2] and A. O. Adeyeye[1,*]
[1]*Information Storage Materials Laboratory, Department of Electrical and Computer Engineering, National University of Singapore, Singapore 117576*
[2]*School of Physics and Astrophysics, University of Western Australia, Crawley, Western Australia 6009, Australia*

(Received 11 January 2017; revised manuscript received 8 May 2017; published 22 June 2017)

A systematic investigation of the magnetization reversal and the dynamic behaviors of uncoupled $Ni_{80}Fe_{20}$ nanowires (NWs) with artificial continuous width modulation is presented. In contrast with the single resonance mode observed in the homogeneous NWs from the broadband ferromagnetic resonance spectroscopy, the NWs with continuous width modulation display three to five distinct resonance modes with increasing wire thickness in the range from 5 to 70 nm due to the nonuniform demagnetizing field. The highest frequency mode and the frequency difference between the two distinct highest modes are shown to be markedly sensitive to the NW thickness. Interestingly, we found that these modes can be described in terms of the quantization of the standing spin waves due to confined varied width. In addition, the easy axis coercive field for the width modulated NWs is much higher than homogeneous NWs of the same thickness when less than 70 nm. Our experimental results are in good qualitative agreement with the micromagnetic simulations. The results may find potential applications in the design and optimization of tunable magnonic filters.

DOI: 10.1103/PhysRevB.95.224426

I. INTRODUCTION

The static and dynamic behaviors of ferromagnetic nanowires (NWs), have been subject to extensive explorations in the past few decades due to their great promise for applications in spintronic devices [1,2] and tunable magnonic filters [3], along with the rapid developments in advanced nanofabrication technologies [4]. The magnetization reversal process of NWs is strongly dependent on the applied magnetic field [5], dimensions [6,7], and roughness [8]. Magnetic domain wall (DW) motion along a NW supports many proposals of spin logic devices [9,10], which are likely to use the pinning effects of a notch. Notches can be used either to locate DW positions [11,12] or to boost [13] the propagation of DWs. For microwave properties, it has been reported theoretically [14] and experimentally [15–17] that homogeneous NWs can support artificial band structure for spin waves (called magnons) with a forbidden band where the transmission is impeded, which can be manipulated by tuning the materials [18,19] or the geometrical dimensions [6,20].

It has been shown that geometrical constrictions on micron-scale NWs can be used to tune resonant frequencies of NWs [21]. Lee *et al.* [22] proposed theoretically the design of microwave waveguides using modulated magnetic NWs. Kim *et al.* [23] later showed the design of gigahertz-range spin-wave filter consisting of a serial combinations of various width modulations with different periodicities [23]. Soon afterwards, a rejection frequency band was experimentally observed in a single Permalloy waveguide of a periodically varying width by Chumak *et al.* [24]. The design of magnonic band gap by edge modulation with steplike or sinusoidal edge profiles of micro-sized waveguides [25] and a lossy width modulated reservoir-waveguide structures [26] were also reported. Recently, works on tuning the band structures of one-dimensional width modulated magnonic crystals (MCs) [27] have shown that two or more band gaps appear due to the NW modulation. Most of the studies of nanoscale NWs with modulation reported so far are theoretical with very few detailed experimental results.

In our earlier study, we showed experimentally two distinct resonant modes in nanoscale wires with periodic isolated modulations [16,28]. It has also been reported that the dynamic response of width modulated NWs can be tuned by modifying both the modulation periodicity and the motif [22,29]. Thus, it would be interesting to investigate the magnetization reversal and dynamic behaviors of NWs with continuous width modulation.

In this paper, we have systematically investigated the magnetization reversal and dynamic behaviors of uncoupled $Ni_{80}Fe_{20}$ (Py) NWs with continuous width modulation with thickness in the range from 5 to 70 nm using vibrating sample magnetometer (VSM) and broadband ferromagnetic resonance (FMR) spectroscopy.

We observed that in contrast to the single resonance mode seen in the homogeneous NWs, the continuous width modulated NWs display three to five distinct resonance modes with increasing wire thickness due to the nonuniform demagnetizing field. The highest-frequency mode and the frequency difference between the two distinct highest modes are shown to be markedly sensitive to the NW thickness. We also observed that the easy axis coercive field for the width modulated NWs is much higher than homogeneous NWs of the same thickness when less than 70 nm. Our experimental results are in good qualitative agreement with the micromagnetic simulations.

II. EXPERIMENTAL AND SIMULATION DETAILS

Two sets of $Fe_{80}Ni_{20}$ NW arrays, homogeneous NWs (NWHs) for reference and NWs with continuous width modulation (NWMs), were fabricated for direct comparison. The width of the homogeneous NWHs is 180 nm. They form a periodic array of parallel wires with a period of 400 nm. The widest region of the modulated NWMs is fixed at 220 nm

---

[*] eleaao@nus.edu.sg

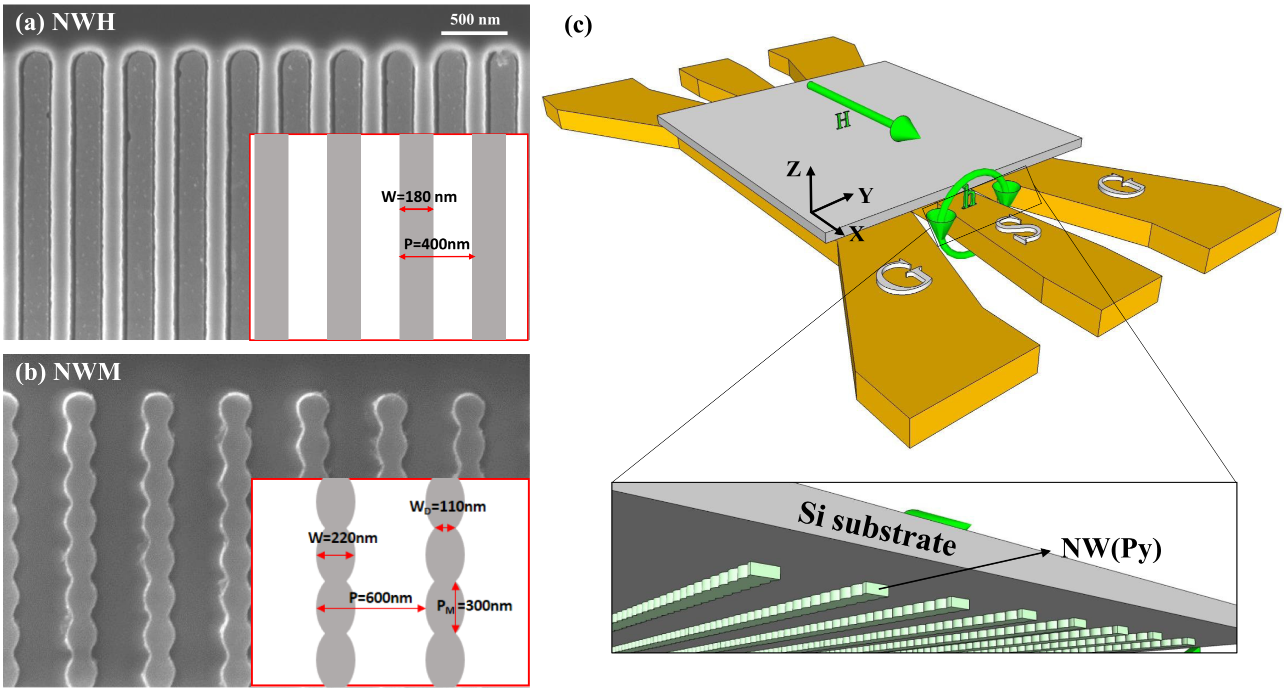

FIG. 1. (a) SEM image for homogeneous NWs with width $W = 180$ nm and period $P = 400$ nm. (b) SEM image for the continuous width modulated NWs with widest width $W = 220$ nm, narrowest width $W_D = 110$ nm and period P = 600 nm. (c) Sketch of the FMR measurement configuration with a sample placed upside down on top of a G-S-G CPW.

and the narrowest region is 110 nm. The period of the width modulation is 300 nm. The wires form a periodic array with a period of 600 nm. The NW arrays were fabricated over an area of $4 \times 4\,\text{mm}^2$ on top of a silicon substrate using deep ultraviolet (DUV) lithography at 193-nm exposure wavelength leading to resist NW arrays. This was followed by deposition of Cr (5 nm)/ $Fe_{80}Ni_{20}$ (t) using electron beam deposition in a vacuum chamber with a base pressure of 2.8×10^{-8} Torr and at rate of 0.2 Å/s. The 5-nm-thick Cr is used to promote good adhesion. The thickness t of the wires is varied in the range from 5 to 70 nm. This was followed by a liftoff process in a resist thinner (OK 73) solution. Details of the fabrication procedures have been described elsewhere [4]. A scanning electron microscope (SEM) was used to verify the completion of the liftoff process and image the dimensions of the NWs. Representative SEM images of the NWs are shown in Figs. 1(a) and 1(b). For the modulated NWs with a field applied along the wire axis, according to Goode and Rowlands [30], the value of β is around $0.4 \sim 0.6$ and α tends to infinity when the thickness of the modulated NWs is 70 nm, leading to fitting factors of the magnetostatic energy approximation from cylinders to rectangles close to 1. Therefore, we can assume that the magnetostatic energy of the width modulated NWs is a good approximation to elliptic cylinders for both flat and curved charge surfaces in our work. If we treat all the wire arrays as a one-dimensional array of cylindrical wires, the minimum ratio of interwire spacing versus largest diameter (when wire thickness is 70 nm) is 2.3. In this case, the magnetostatic coupling between the wires can be ignored [31].

The collective magnetization reversal processes of the arrays were characterized at room temperature using VSM by sweeping the magnetic field along the easy axis of the NWs. The dynamic behaviors of the NW arrays were investigated using FMR. To obtain the high-frequency response, a vector network analyzer (VNA) is connected to a 50 Ohm coplanar waveguide (CPW) using two ground-signal-ground (G-S-G) type microwave Picoprobes. The signal line of the CPW is 8 mm long and 20 μm wide. The gap between ground and signal line is 50 μm. The samples were placed upside down on top of the CPW. The radio frequency (RF) currents pass through the waveguide and generate magnetic field h_{rf} along the Y direction (the hard axis of the NWs) to excite the magnetization. Due to the finite size of the signal line, the h_{rf} is not homogeneous in the Y direction. However, continuity of the probed material is broken in the Y direction by its nanostructuring. Therefore, excitation of traveling spin waves is excluded [32]. Excluded also is excitation of Bloch spin waves [33] because of the distance between individual wires is on the order of the free propagation path for the Bloch waves. The latter implies that the driving microwave field couples to each of the wires individually but coherently. Therefore, the total FMR response of the array represents a sum of identical FMR responses of individual wires with individual complex amplitudes depending on wire position with respect to the RF field nonhomogeneity. As this is a sum of coherent signals at the same frequency, no influence on the FMR peak position and linewidth is expected. Here, one has to note that the contribution of the out-of-plane component of the driving field to the total FMR response is much more significant than for continuous films [34]. For the coplanar geometry, it may be particularly strong, because of strong concentration of the out-of-plane RF field in the gaps between the S- and G-lines of a CPW. An external static magnetic field H_{app} was applied along the easy axis of the NWs, i.e., along the X

direction. The 3D sketch of FMR configuration is shown in Fig. 1(c). The transmission parameter S_{21} of the VNA was measured at room temperature by sweeping the frequency in the range from 10 MHz to 20 GHz at a fixed applied field H_{app}. The measurement was repeated for a series of H_{app} values from negative saturation ($H_{\mathrm{app}} = -1400$ Oe), passed through 0 Oe and then gradually increased to positive saturation field ($H_{\mathrm{app}} = +1400$ Oe).

In order to understand the dynamic response of the wires, micromagnetic simulations were performed using the LLG micromagnetic simulator [35], which computes the equilibrium magnetization distribution of the NWs based on the Landau-Lifshitz-Gilbert (LLG) equation:

$$\frac{\partial \boldsymbol{m}}{\partial t} = -\gamma \boldsymbol{m} \times \boldsymbol{H}_{\mathrm{eff}} + \alpha \boldsymbol{m} \times \frac{\partial \boldsymbol{m}}{\partial t}, \qquad (1)$$

where $\boldsymbol{m}$ is the unit vector of local magnetization, γ is the gyromagnetic ratio, $\boldsymbol{H}_{\mathrm{eff}}$ is the effective field, and α is the Gilbert damping constant. The masks used in the simulations were all directly extracted from the SEM images shown in Figs. 1(a) and 1(b). Standard material parameters for Py were used: saturation magnetization $M_s = 860\ \mathrm{emu/cm^3}$, exchange stiffness $A = 1.3 \times 10^{-6}$ erg/cm, magnetocrystalline anisotropy $K_u = 0$, and a unit cell size of $5 \times \mathrm{nm}\,5\,\mathrm{nm} \times 5\,\mathrm{nm}$. To identify different resonance modes, dynamic simulations were performed using a gyromagnetic ratio $\gamma = 2.8$ GHz/kOe and damping constant $\alpha = 0.008$. The resonant mode profiles were extracted using spatially and frequency-resolved Fast-Fourier-Transform (FFT) imaging method [36]. In all the simulations, periodic boundary condition was used to mimic the wire arrays.

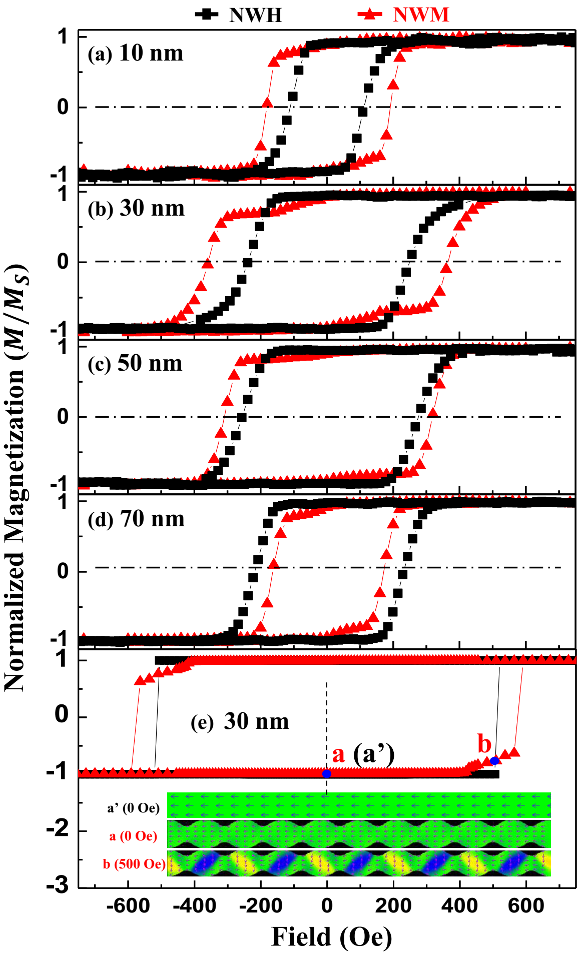

FIG. 2. (a)–(d) Experimental hysteresis loops for NWHs and NWMs taken at different thickness in the range from 10 to 70 nm. (e) Simulated hysteresis loops for 30 nm NWH and NWM. (Inserts are the magnetization states at $H_{\mathrm{app}} = 0$ Oe for NWH and NWM and $H_{\mathrm{app}} = 500$ Oe for NWM.)

III. RESULTS AND DISCUSSION

Shown in Figs. 2(a)–2(d) are the representative magnetic hysteresis loops for NWHs and NWMs as a function of the film thickness. We observed that when the film thickness is less than 70 nm, the coercive field of NWMs is significantly larger than NWHs with the same film thickness. For example, when $t = 10$ nm, the coercive field is 184 Oe for NWM and 108 Oe for NWH. This can be explained by the different demagnetizing fields due to much smaller dimension at the narrowest region of the NWMs compared to the NWHs for thin films [37]. Interestingly, we observed that the coercive field for both the wire arrays first increases and then decreases with the increase of the film thickness. For NWHs, the coercive field increases from 108 Oe to 252 Oe when t is increased from 10 nm to 50 nm, and then decreases to 216 Oe at $t = 70$ nm. This is caused by the transition from coherent dominated reversal mode to curling magnetization when the thickness keeps increasing, which is in good qualitative agreement with previous results [38]. For NWMs, the coercive field first increases from 184 Oe at $t = 10$ nm to 357 Oe at $t = 30$ nm and then drops to 163 Oe at $t = 70$ nm. This is probably due to the formation of complex vortex DWs inside the NWs when the thickness increases and is comparable to its narrowest width [39]. Two-step switching can be observed for the width modulated NWs, it is caused by the modulation induced domain wall pinning effect. As shown in Fig. 2(e), the magnetization state for the NWMs at 500 Oe indicates that domain walls form around the narrowest region due to width modulation. The representative simulated hysteresis loops for 30 nm NWHs and NWMs are also shown in Fig. 2(e) and they agree well with the experiments. The magnetization states at remanence at the bottom show that no switching occurs at $H_{\mathrm{app}} = 0$ Oe, which is consistent with measured hysteresis loops.

Figures 3(a) and 3(b) show the representative absorption curves of the NWs for both homogeneous NWs and NWs with continuous width modulation taken at remanence ($H_{\mathrm{app}} = 0$ Oe) as a function of film thickness in the range from 5 to 70 nm. As expected, the resonance mode of all the homogeneous NWs is characterized by the domination of one single peak as shown in Fig. 3(a) and the resonant frequency increases with the thickness of the wires, which can be explained by Kittel's equation [40]:

$$w_0 = \gamma\sqrt{[H_x + (N_{zz} - N_{xx})4\pi M_x] \times [H_x + (N_{yy} - N_{xx})4\pi M_x]}, \qquad (2)$$

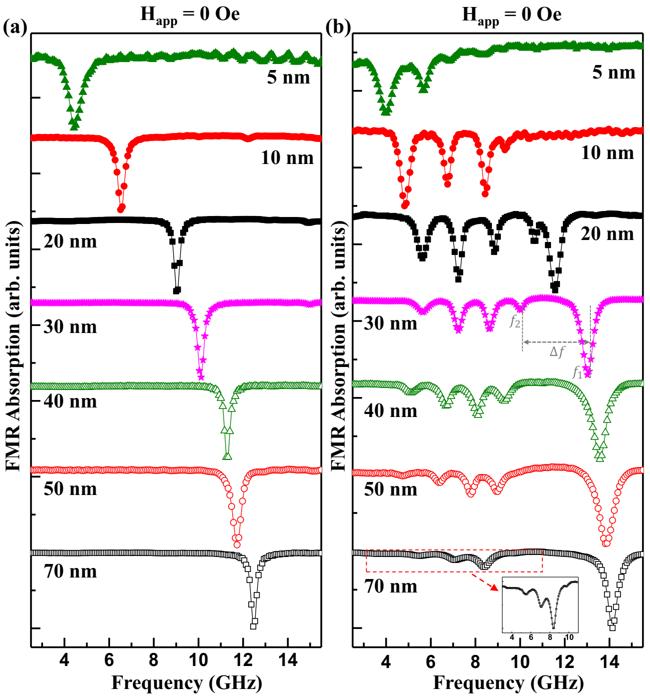

FIG. 3. Experimental absorption spectra for (a) homogeneous NWHs and (b) width modulated NWMs at remanence ($H_{app} = 0$ Oe) as a function of $Ni_{80}Fe_{20}$ thickness (t) in the range from 5 to 70 nm. The inset is the zoom-in spectra for 70-nm NWMs with the frequency ranging from 3 to 11 GHz.

where N_{xx}, N_{yy}, and N_{zz} are the effective demagnetizing factors along wire length, width, and thickness, respectively, H_x is the applied external field, and M_x is the magnetization along X direction. Intriguingly, for the width modulated NWs, three to five resonant modes are observed and the number of modes increases as the thickness of the NWMs is increased. Three modes were found at 4.0 GHz, 5.8 GHz, and 6.8 GHz for $t = 5$ nm. The number of resonance modes increased to five (at 5.6 GHz, 7.2 GHz, 8.6 GHz, 10.0 GHz, and 13.0 GHz) when t is increased to 30 nm.

We also observed that the frequency difference Δf between the highest mode f_1 and the second highest mode, defined as f_2, increases with the wire thickness. The difference is $\Delta f = 3$ GHz when $t = 30$ nm and $\Delta f = 5.8$ GHz when $t = 70$ nm. It can also be seen that the absorption intensity of the lower modes gradually decreases when the thickness of the NWs increases compared to the relative increase of the highest mode.

Figure 4 shows the experimental two-dimensional (2D) FMR absorption spectra for the forward half of the hysteresis loop with H_{app} varying from -500 Oe to +500 Oe as a function of $Ni_{80}Fe_{20}$ thickness for both the homogeneous NWHs and NWMs with continuous width modulation, respectively. Consistent with Fig. 3(a), for all thickness, only a single absorption mode was observed for the homogeneous NWHs and the sharp frequency jump shows a typical hysteresis phenomenon. The effect of the width modulation and the increase of the NW thickness is apparent comparing Figs. 4(a) and 4(b). Three distinct modes appear at $t = 5$ nm, and four modes when t is increased to 10 nm. Five modes can be observed when t is increased to 30 and 50 nm. The resonant modes also shift to higher frequencies as NW thickness is increased, which agrees well with previous results [16,28] and can be interpreted using the Kittel's equation [40] due to the change of the demagnetizing factors. The strong dependence of the frequency difference Δf on the thickness of the wires is evident in the 2D spectra.

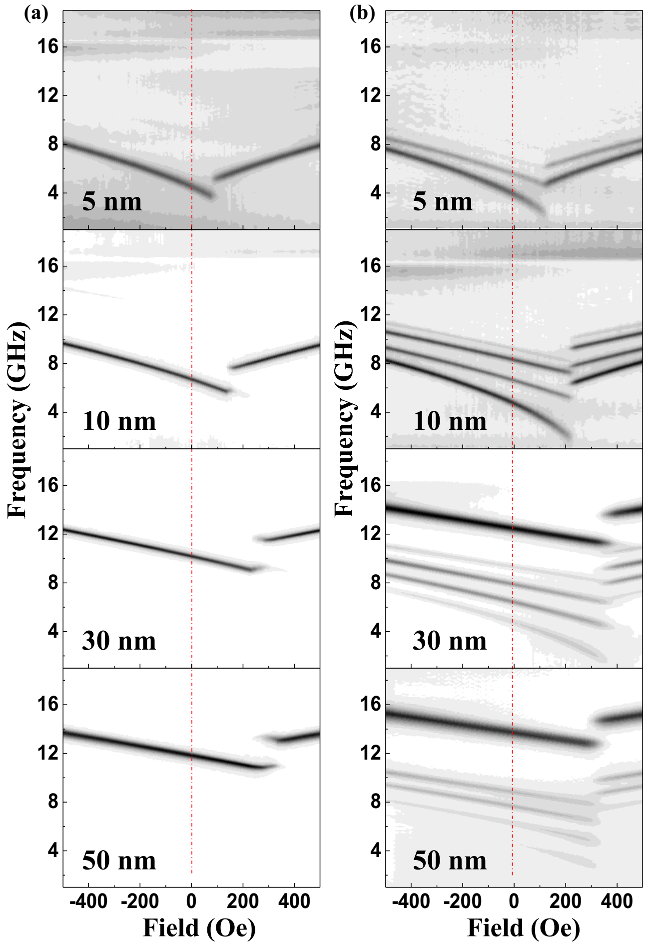

FIG. 4. Experimental 2D FMR spectra for (a) homogeneous NWHs and (b) width modulated NWMs with $Ni_{80}Fe_{20}$ thickness $t = 5$ nm, $t = 10$ nm, $t = 30$ nm, and $t = 50$ nm.

To gain deeper insights about the experimental FMR results, dynamic micromagnetic simulations have been carried out on both the homogeneous NWHs and the NWMs with width modulation. Shown in Figs. 5(a) and 5(b) are the simulated FMR absorption curves for both the two types of NWs as a function of thickness at remanence state ($H_{app} = 0$ Oe). There is a good qualitative agreement between the experimental resonance modes and the micromagnetic simulations in terms of the features of the number of modes, profile and frequency range. We observed all the prominent modes in the simulated spectra in agreement with the experimental results. For the 30-nm-thick NWs with width modulation, five modes were observed experimentally and the resonant frequencies are 5.6 GHz, 7.2 GHz, 8.6 GHz, 10.0 GHz, and 13.0 GHz. In the simulation, five distinct modes can be observed at frequencies 6.1 GHz, 7.2 GHz, 8.4 GHz, 9.6 GHz,

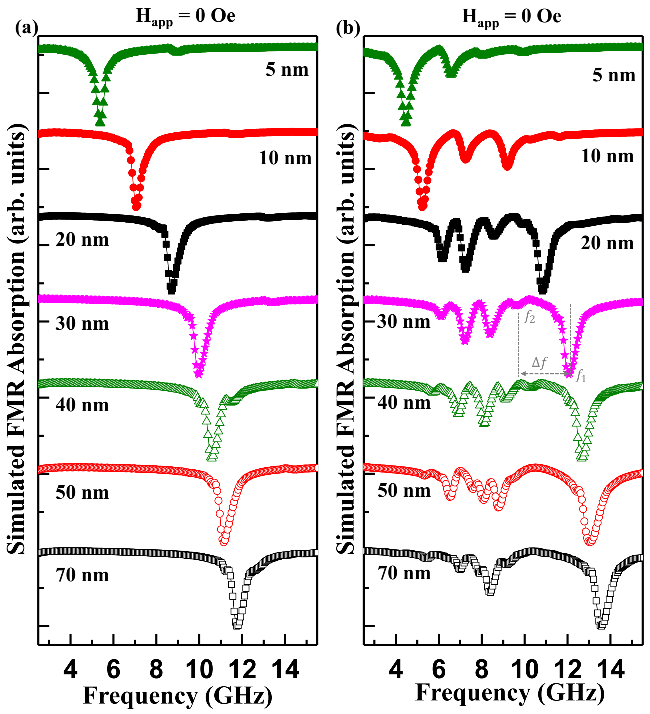

FIG. 5. Simulated FMR absorption spectra for (a) homogeneous NWHs and (b) width modulated NWMs at remanence ($H_{app} = 0$ Oe) as a function of $Ni_{80}Fe_{20}$ thickness (t) in the range from 5 to 70 nm.

and 12 GHz. One possible reason for the noticeable difference between the simulation and the real experiment is the surface roughness or inhomogeneity of the modulated nanowires, which may change the demagnetizing factors in magnetic thin films [8].

To identify the FMR modes at each resonant frequency, we have further extracted and plotted their spatial profiles in terms of the local absorbed power. The representative mode profiles for the 30-nm homogeneous NWHs and width-modulated NWMs as a function of thickness are shown in Fig. 6. The red color indicates a high spin precession amplitude and therefore high absorption, whereas the blue color corresponds to low absorption. We found that the mode at 10 GHz for 30 nm NWHs is distributed homogeneously along the whole wires, which is similar to that of the NWHs with different thicknesses. For the width-modulated NWMs with various thicknesses, we found that the highest mode is concentrated at the narrowest region and the lowest mode is located at the widest region. If we assign "local" effective demagnetizing factors to different sections of the unit cell of the NWMs, the narrow areas will be characterized by the largest dynamic in-plane factor N_{yy}, as the aspect ratio thickness/width is the largest for this section of the unit cell. Also, the width of this section is small enough to expect a nonnegligible contribution from the inhomogeneous exchange interaction to the mode frequency. For these two reasons, one may expect the largest FMR frequency for the fundamental (single-anti-node) mode of this area. Similarly, N_{yy} for the wider sections of the NWMs is the smallest one and the exchange contribution to the eigen-frequency is also the smallest, therefore the fundamental mode of these areas has the lowest frequency (4.5, 5.2, 6.1, and 6.5 GHz for $t = 5$, 10, 30, and 50 nm, respectively).

The next-order mode is a mode having three antinodes over the wider sections of the unit cell. This is best seen for $t = 10$ nm (the respective frequency is 7.2 GHz), but also evident for $t = 30$ and 50 nm (7.2 and 8.0 GHz, respectively). Noteworthy is that the largest NWM thickness (50 nm) allows existence of one more excitation at a frequency (7.6 GHz) between the ones for the fundamental and the three-antinode modes. At the first glance, this mode looks like a two-antinode mode, however excitation of the two-antinode mode by a spatially uniform field must be prohibited for symmetry reason, as the magnetization vector for a true two-antinode

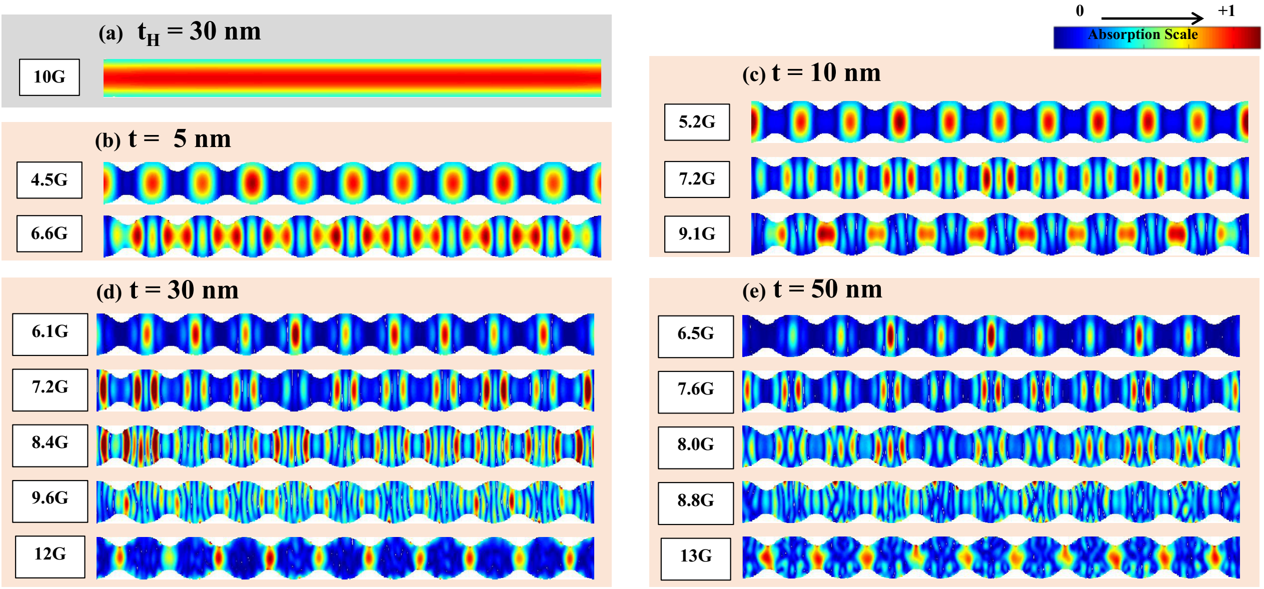

FIG. 6. Simulated mode profiles for (a) 30-nm homogeneous NWHs and (b)–(e) width modulated NWMs with $Ni_{80}Fe_{20}$ thickness $t = 5$ nm, $t = 10$ nm, $t = 30$ nm, and $t = 50$ nm at remanence ($H_{app} = 0$ Oe).

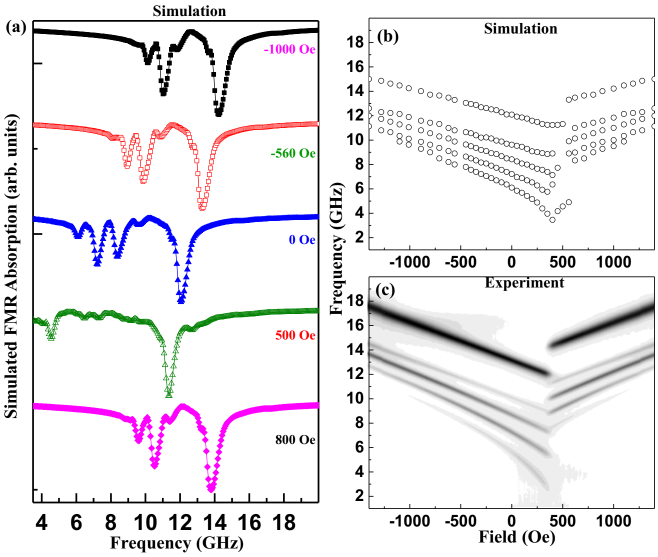

FIG. 7. (a) Simulated FMR absorption curves for 30-nm-width modulated NWMs at various fields, $H_{\text{app}} = -1000$ Oe, -560 Oe, 0 Oe, 500 Oe, and 800 Oe. (b) The simulated 2D absorption spectra and (c) the experimental 2D FMR results for the 30-nm-width modulated NWMs as a function of the applied field from -1400 Oe to 1400 Oe.

mode should precess in antiphase for the antinodes. Therefore, this mode is more likely to be a three antinode mode with the amplitude of the central antinode strongly suppressed. Indeed, for $t = 30$ nm, one sees that the amplitude of the central antinode for the 7.2 GHz mode is noticeably smaller than the other two antinodes, although the three antinodes have almost the same amplitudes for $t = 10$ nm at 7.2 GHz. This suggests that there is a gradual decrease in the amplitude of the central antinode with an increase in t, possibly related to an increase in the areal nonuniformity of the static magnetization and internal field of the wider area with the increase in t. Also comparing the profiles of the 7.6 GHz mode for $t = 50$ nm with the one for the next order mode (8.0 GHz), one may conclude that for this t value the three-antinode mode splits into two excitations—the three-antinode one with the suppressed central antinode (at 7.6 GHz) and a one which looks like as a hybrid of three-antinode and five-antinode distributions (8.0 GHz). This "pure mode" hybridization becomes possible due to the periodic nonuniformity of the static magnetic parameters along the NWM length combined with periodic modulation of dynamic magnetization in the same direction.

Similarly, the remainder of the modes seen in Fig. 6 represents more complex standing-wave patterns in the X direction. Alternatively, they may be thought as higher-order Bloch spin waves on such a periodic spin wave waveguide. These Bloch waves are standing, because FMR can only excite standing-wave modes, and for a periodic medium, as in our case, these should be excitations in the center of the first Brillouin zone.

To better understand the dynamic responses as a function of the applied field, we simulated the absorption curves for the forward half loop starting from -1400 Oe to 1400 Oe for the 30 nm width modulated NWMs. Shown in Fig. 7(a) are the simulated FMR absorption spectra at different applied magnetic fields. For the field region away from the switching field at around 500 Oe, five modes can be observed. At $H_{\text{app}} = 500$ Oe, only the major mode is distinct, the lower frequency modes are vastly different from the other fields due to significant changes in the magnetization state during the switching process. The weak peaks at $H_{\text{app}} = 500$ Oe are all shown in the simulated 2D FMR absorption spectra in Fig. 7(b). The simulated spectra in Fig. 7(b) coincide with the experimental result in Fig. 7(c).

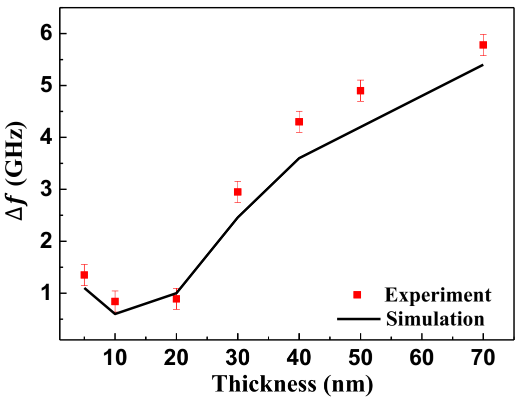

FIG. 8. Extracted experimental and simulated frequency difference Δf between the two highest resonant modes for width modulated NWMs as a function of the film at remanence ($H_{\text{app}} = 0$ Oe).

We define the frequency difference between the two highest resonant modes as $\Delta f = f_1 - f_2$ and further extracted the experimental and simulated frequency difference Δf as a function of the wire thickness for the width modulated NWMs at remanence and plot the curves in Fig. 8. The error bar for the experimental result shows that there is no significant statistic difference in various measurements. There is a good qualitative agreement in terms of trend between the experiment and the simulation. We observed that the difference Δf is strongly dependent on the thickness of the wires for $t > 10$ nm, which increases with the thickness when thickness is no less than 10 nm. This is due to the marked modification in the demagnetizing factors as discussed above.

We have thus shown that the magnetization reversal mechanism and the dynamic responses of ferromagnetic NWs can be easily tuned by introducing controlled width modulation as well as varying the thickness of the NWs. It has been shown that the number of modes, the resonant frequencies and the mode profiles change with the thickness of the NWs when artificial continuous width modulation has been introduced. In addition, the easy axis coercive field for the width modulated NWs is much higher than homogeneous NWs of the same thickness when less than 70 nm. The findings in this work may find useful applications in designing microwave filters and signal processing.

IV. CONCLUSION

We have investigated the static and dynamic behaviors of uncoupled $Ni_{80}Fe_{20}$ NWs with artificial continuous width modulation as a function of the film thickness. In contrast with the single resonance mode observed in the homogeneous NWs, the NWs with continuous width modulation display three to five distinct resonance modes with increasing wire thickness in the range from 5 to 70 nm due to nonuniform demagnetizing field. The highest frequency mode and the frequency difference between the two distinct highest modes are very sensitive to the NW thickness. We found that these modes can be described in terms of the quantization of the standing spin waves due to confined varied width. In addition, the easy axis coercive field for the width modulated NWs is much higher than homogeneous NWs of the same thickness when less than 70 nm. Our experimental results are in good qualitative agreement with the micromagnetic simulations.

ACKNOWLEDGMENT

This work was supported by National Research Foundation, Prime Minister's Office, Singapore under its Competitive Research Programme (CRP Award No. NRF-CRP 10-2012-03). A.O.A. is a member of the Singapore Spintronics Consortium (SG-SPIN).

[1] S. P. S. Parkin, M. Hayashi, and L. Thomas, Science **320**, 190 (2008).
[2] D. A. Allwood, G. Xiong, C. C. Faulkner, D. Atkinson, D. Petit, and R. P. Cowburn, Science **309**, 1688 (2005).
[3] S. Choi, K.-S. Lee, K. Y. Guslienko, and S.-K. Kim, Phys. Rev. Lett. **98**, 087205 (2007).
[4] S. Navab, S. Goolaup, and A. O. Adeyeye, Nanotechnology **15**, 1539 (2004).
[5] J. Ding and A. O. Adeyeye, Adv. Func. Mater. **23**, 1684 (2013).
[6] S. Goolaup, A. O. Adeyeye, N. Singh, and G. Gubbiotti, Phys. Rev. B **75**, 144430 (2007).
[7] S. Goolaup, N. Singh, and A. O. Adeyeye, Nanotechnology: IEEE Trans. **4**, 523 (2005).
[8] Y.-P. Zhao, R. M. Gamache, G.-C. Wang, T.-M. Lu, G. Palasantzas, and J. T. M. De Hosson, J. Appl. Phys. **89**, 1325 (2001).
[9] A. Imre, G. Csaba, L. Ji, A. Orlov, G. H. Bernstein, and W. Porod, Science **311**, 205 (2006).
[10] L. Gross, R. R. Schlittler, G. Meyer, and R. Allenspach, Nanotechnology **21**, 325301 (2010).
[11] D. Atkinson, D. S. Eastwood, and L. K. Bogart, Appl. Phys. Lett. **92**, 022510 (2008).
[12] T.-C. Chen, C.-Y. Kuo, A. K. Mishra, B. Das, and J.-C. Wu, Phys. B: Condens. Matter **476**, 161 (2015).
[13] H. Y. Yuan and X. R. Wang, Phys. Rev. B **92**, 054419 (2015).
[14] J. Ding, M. Kostylev, and A. O. Adeyeye, Phys. Rev. B **84**, 054425 (2011).
[15] J. Ding, M. Kostylev, and A. O. Adeyeye, Phys. Rev. Lett. **107**, 047205 (2011).
[16] L. L. Xiong and A. O. Adeyeye, Appl. Phys. Lett. **108**, 262401 (2016).
[17] B. K. Kuanr, R. Lopusnik, L. M. Malkinski, M. Wenger, M. Yu, D. Scherer, R. E. Camley, and Z. Celinski, J. Appl. Phys. **103**, 07C508 (2008).
[18] S. Mamica, M. Krawczyk, M. L. Sokolovskyy, and J. Romero-Vivas, Phys. Rev. B **86**, 144402 (2012).
[19] Z. K. Wang, V. L. Zhang, H. S. Lim, S. C. Ng, M. H. Kuok, S. Jain, and A. O. Adeyeye, Appl. Phys. Lett. **94**, 083112 (2009).
[20] G. N. Kakazei, X. M. Liu, J. Ding, and A. O. Adeyeye, Appl. Phys. Lett. **104**, 042403 (2014).
[21] S. Lepadatu, O. Wessely, A. Vanhaverbeke, R. Allenspach, A. Potenza, H. Marchetto, T. R. Charlton, S. Langridge, S. S. Dhesi, and C. H. Marrows, Phys. Rev. B **81**, 060402 (2010).
[22] K.-S. Lee, D.-S. Han, and S.-K. Kim, Phys. Rev. Lett. **102**, 127202 (2009).
[23] S.-K. Kim, K.-S. Lee, and D.-S. Han, Appl. Phys. Lett. **95**, 082507 (2009).
[24] A. V. Chumak *et al.*, Appl. Phys. Lett. **95**, 262508 (2009).
[25] F. Ciubotaru, A. V. Chumak, N. Y. Grigoryeva, A. A. Serga, and B. Hillebrands, J. Phys. D: Appl. Phys. **45**, 255002 (2012).
[26] M. Arikan, Y. Au, G. Vasile, S. Ingvarsson, and V. V. Kruglyak, J. Phys. D: Appl. Phys. **46**, 135003 (2013).
[27] K. Di, H. S. Lim, V. L. Zhang, S. C. Ng, M. H. Kuok, H. T. Nguyen, and M. G. Cottam, J. Appl. Phys. **115**, 053904 (2014).
[28] J. Ding, V. E. Demidov, M. G. Cottam, S. O. Demokritov, and A. O. Adeyeye, Appl. Phys. Lett. **104**, 143105 (2014).
[29] P. J. Metaxas, M. Albert, S. Lequeux, V. Cros, J. Grollier, P. Bortolotti, A. Anane, and H. Fangohr, Phys. Rev. B **93**, 054414 (2016).
[30] D. A. Goode and G. Rowlands, J. Magn. Magn. Mater. **267**, 373 (2003).
[31] K. Y. Guslienko, Appl. Phys. Lett. **75**, 394 (1999).
[32] G. Counil, J.-V. Kim, T. Devolder, C. Chappert, K. Shigeto, and Y. Otani, J. Appl. Phys. **95**, 5646 (2004).
[33] M. P. Kostylev and A. A. Stashkevich, Phys. Rev. B **81**, 054418 (2010).
[34] C. S. Chang, M. Kostylev, A. O. Adeyeye, M. Bailleul, and S. Samarin, Europhys. Lett. **96**, 57007 (2011).
[35] M. R. Scheinfein and E. A. Price, LLG Micromagnetics Simulator, software for micromagnetic simulations, http://llgmicro.home.mindspring.com (last access: 09/09/2015).
[36] M. Buess, R. Höllinger, T. Haug, K. Perzlmaier, U. Krey, D. Pescia, M. R. Scheinfein, D. Weiss, and C. H. Back, Phys. Rev. Lett. **93**, 077207 (2004).
[37] A. Ercole, A. O. Adeyeye, C. Daboo, J. A. C. Bland, and D. G. Hasko, J. Appl. Phys. **81**, 5452 (1997).
[38] S. Goolaup, N. Singh, A. O. Adeyeye, V. Ng, and M. B. A. Jalil, Eur. Phys. J. B **44**, 259 (2005).
[39] V. Estévez and L. Laurson, Phys. Rev. B **93**, 064403 (2016).
[40] C. Kittel, Phys. Rev. **73**, 155 (1948).